

Novel Water-Splitting Electrolyzer Design Incorporating a Gas Diffusion Electrode and a Gel Membrane for Highly Efficient Hydrogen Production

Fajun Li,* Huaizhu Wang, Guizhi Wang, Min Ding, Qihui Ma, Haifeng Xu,* and Zhong Jin*



Cite This: *Langmuir* 2024, 40, 17109–17117



Read Online

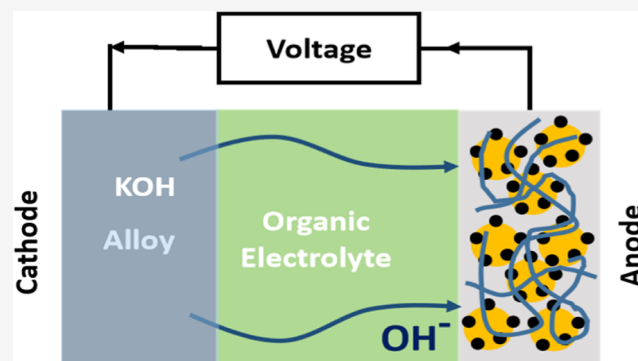
ACCESS |

Metrics & More

Article Recommendations

Supporting Information

ABSTRACT: Advancements in cost-effective, high-performance alkaline water-splitting systems are crucial for the hydrogen industry. While the significance of electrode material design has been widely acknowledged, the practical implementation of these advancements remains challenging. In this study, we focused on the holistic design of the electrolysis system and successfully developed a novel alkaline water-splitting electrolyzer. The unique configuration of our electrolyzer allows the designed NiFe-LDH/carbon cloth gas diffusion anode to interact solely with the PVA-based gel membrane and air, enabling the direct discharge of oxygen into the gas phase. This innovative feature accelerates anode bubble overflow, reduces gas interference, and decreases the system impedance by minimizing electrode spacing. As a result, by utilizing the NiFeSn-alloy/nickel mesh cathode, our electrolyzer achieves a high current density of 308 mA cm^{-2} at a cell voltage of 2.0 V and demonstrates exceptional stability over 1000 h.



INTRODUCTION

As escalating energy demand and increasing fossil fuel consumption intensify, the focus on the development of renewable, clean, and sustainable energy sources is ever-growing.^{1,2} Hydrogen production via water electrolysis presents a cost-effective and promising method to address this energy challenge.^{3–5} Nevertheless, this system, comprising anode oxygen evolution reaction (OER) and cathodic hydrogen evolution reaction (HER), has been severely impeded due to high reaction barriers.^{6,7} The application of electrocatalysts can significantly lower these barriers, thereby accelerating the kinetic transfer reactions inherent in the HER/OER process.⁸ Yet, the prevalent catalysts are predominantly composed of precious metals like Pt and Ru/Ir-based materials, which, despite their effective catalytic properties under basic conditions, are hampered by their high cost and scarcity.^{9–13} Therefore, the urgency for meticulously designed efficient catalyst electrodes for overall water splitting is paramount.^{14,15} Various electrocatalysts have been crafted using diverse physical and chemical methodologies, including pulsed laser deposition, hydrothermal/solvothermal treatment, coprecipitation, and electrodeposition, each offering its own unique set of benefits.^{16–19} Furthermore, the strategic design of the electrode has proven crucial for enhancing performance, with a plethora of catalytic electrodes based on porous conductive substrates [such as nickel foam, copper foil, and carbon cloth (CC)] demonstrating high current densities at

low potentials.^{20–24} Notably, NiFe-LDH-based materials have exhibited superior performance and stability as OER electrocatalysts, albeit their application is constrained due to their low electrical conductivity and intrinsic dearth of active sites.^{25–27} For instance, Wang et al.²⁸ successfully fabricated self-supporting NiFe-LDH on Cu mesh, achieving a high current density of 600 mA cm^{-2} at a relatively low overpotential for OER. Nanostructures have also been found to augment the catalytic activity and durability of water splitting through the facilitation of material transport, alteration of electronic structure, exposure of large active sites, and enhancement of surface reactivity.^{29–31} Zhou et al.³² demonstrated this by constructing a core–shell structure with crystalline CuO nanorods as the core and an amorphous NiFe-LDH shell, attaining a current density of 50 mA cm^{-2} with a mere 290 mV overpotential.

Transition metal-based alloys such as Ni–Co, Ni–Fe, Ni–Mo, and Ni–Cu have shown excellent electrocatalytic performance in water splitting for HER, owing to their high electronic conductivity and robust stability.^{18,33–39} The

Received: June 7, 2024

Revised: July 16, 2024

Accepted: July 24, 2024

Published: July 30, 2024



integration of Ni with other metals to form bimetallic alloys significantly enhances their inherent electrocatalytic activity and resistance to corrosion.^{40,41} Sun et al.⁴² crafted NiCo alloys of varying proportions for the HER through chemical deposition, reaching a current density of 10 mA cm^{-2} with just 52 mV overpotential. Another crucial factor that boosts the catalytic activity is the conductivity and surface area of the catalyst, which in turn accelerate mass transfer, promote electrolyte diffusion, and facilitate bubble release.^{37,43} Zhou et al.⁴⁴ demonstrated this via preparing a 3D-layered NiFe metal foam electrode by electrodeposition on a copper sheet. Similarly, Teng et al.⁴⁵ produced NiFe and NiCo catalysts on nickel foam for overall water electrolysis, managing to maintain a working voltage of only 1.73 V even when the current density was 500 mA cm^{-2} .

The dominant technologies for water electrolysis currently are alkaline water electrolysis (AWE) and proton exchange membrane (PEM) electrolysis. AWE, being the oldest, most mature, and most widely commercialized method for hydrogen production, consists of a pair of electrodes immersed in an alkaline solution, with gases being separated by a central diaphragm.^{46,47} Current diaphragms are primarily composed of glass fiber-reinforced polyphenylene sulfide or polysulfone, possessing high chemical and thermal stability.⁴⁸ On the other hand, PEM electrolysis, albeit not as mature as AWE, uses an acidic polymer electrolyte membrane for efficient transport of proton H^+ and necessitates the use of precious metal catalysts and costly electrolyte membranes, thus increasing the cost of hydrogen production.^{49,50} A promising alternative under development is a new alkaline electrolyzer using an anion-exchange membrane to replace PEM electrolysis, whereby the membrane transports the anion OH^- rather than proton H^+ .⁵¹ This approach integrates the advantages of PEM and AWE, enabling the use of affordable transition metal catalysts and diaphragm materials to produce high purity hydrogen with minimal energy consumption. However, the diaphragm's durability still presents a challenge and continues to be under development. In industry-standard alkaline electrolyzers, a 30 wt % KOH solution is used as the electrolyte, and the numerous bubbles formed on the electrode surface during operation can cover the electrode surface, thereby reducing the active area. To address this, we designed an electrolysis device with a gas diffusion electrode and a gel material diaphragm. In comparison to traditional alkaline electrolyzers, this setup offers several advantages: first, the gel material lowers the diaphragm resistance; second, the generated oxygen is directly separated into the atmosphere, mitigating the anode bubble's resistance; and third, reducing the electrode spacing enhances ion and mass transport.

In this study, we have successfully fabricated highly conductive and durable electrodes via a simple method that promotes electron transport and gas diffusion to mitigate the effect of bubbles generated during water splitting. Additionally, the organic-gel PVA membrane, which undergoes freezing self-cross-linking, serves as a supportive element, imparting strength, toughness, and flexibility while ensuring high ionic conveyance. Based on these materials, we established an alkaline water electrolyzer using NiFeSn-alloy/nickel mesh (NM) and NiFe-LDH/CC as the cathode and anode, respectively. This setup yields a current density of 308 mA cm^{-2} at 2.0 V with remarkable stability. This research represents a significant step toward practical application in the field of water splitting.

EXPERIMENTAL SECTION

Chemicals. $\text{NiSO}_4 \cdot 6\text{H}_2\text{O}$, $\text{FeSO}_4 \cdot 7\text{H}_2\text{O}$, SnSO_4 , H_3BO_3 , NaCl , KOH , HCl , $\text{C}_6\text{H}_5\text{Na}_3\text{O}_7 \cdot 2\text{H}_2\text{O}$, $\text{Ni}(\text{NO}_3)_2 \cdot 6\text{H}_2\text{O}$, $\text{Fe}(\text{NO}_3)_3 \cdot 9\text{H}_2\text{O}$, NH_4F , and urea were purchased from the Aladdin Company. Nafion solution (5 wt %) was purchased from Aldrich. Poly(vinyl alcohol) (PVA) was purchased from Sinopharm Chemical Reagent Co., Ltd. All reagents were of analytical grade and used without further purification.

Prior to experimentation, both the NM and CC were subjected to ultrasonic cleaning with a solution of 3.0 M HCl, ethanol, and distilled water for a duration of 15 min to remove the surface oxide layer and impurities.

Preparation of NiFeSn-Alloy/NM Electrode. The NiFeSn-alloy/NM was prepared via an electrodeposition method within a two-electrode system. $\text{NiSO}_4 \cdot 6\text{H}_2\text{O}$ (40 mmol), $\text{FeSO}_4 \cdot 7\text{H}_2\text{O}$ (10 mmol), SnSO_4 (2.5 mmol), H_3BO_3 (30 mmol), NaCl (50 mmol), and $\text{C}_6\text{H}_5\text{Na}_3\text{O}_7 \cdot 2\text{H}_2\text{O}$ (24 mmol) were dissolved into 100 mL of deionized water to form a homogeneous solution. Oxygen was effectively removed by introducing Ar to mitigate its negative effect. Throughout the electrodeposition process, the precleaned NM and graphite electrodes were utilized as the working and counter electrodes, respectively, within the CHI 760E electrochemical analyzer workstation. This was performed at a current density of 20 mA cm^{-2} for 60 min. Post electrodeposition, NiFeSn-alloy/NM was carefully extracted, thoroughly rinsed multiple times with deionized water, and then dried in a vacuum at 60°C .

Preparation of NiFe-LDH/CC Electrode. The NiFe-LDH powder was first prepared by using a hydrothermal method. Briefly, $\text{Ni}(\text{NO}_3)_2 \cdot 6\text{H}_2\text{O}$ (2.0 mmol), $\text{Fe}(\text{NO}_3)_3 \cdot 9\text{H}_2\text{O}$ (0.2 mmol), NH_4F (4.0 mmol), and urea (10.0 mmol) were dissolved into 60 mL of deionized water, then stirred continuously for 10 min. This aqueous solution was transferred into a 100 mL Teflon-lined autoclave and heated to 120°C for 12 h. Once the autoclave reactor cooled to room temperature, the resultant powder was harvested through a series of washing cycles with deionized water and then dried at 60°C for 8 h. To prepare the catalyst ink, 12 mg of the catalyst was dispersed into a solution consisting of 480 μL of ethanol, 500 μL of deionized water, and 20 μL of Nafion (5 wt %), and then subjected to ultrasonication for 30 min. The resulting gas diffusion catalytic electrode, denoted as NiFe-LDH/CC, was prepared with a loading of 0.6 mg cm^{-2} via dispersion of the catalytic ink onto the surface of the CC.

Preparation of the Gel PVA Membrane. PVA (4.0 g) was completely dissolved in deionized water while stirring magnetically at 90°C for 30 min, yielding a uniform solution. The gel PVA membrane was then prepared through the frozen cross-linking method at -20°C for 12 h. This was taken out and left at room temperature for 60 min, a process repeated thrice. Gel PVA membranes of varying mass percentages of PVA (10, 12, 14, and 16%) were also prepared in a similar manner. Lastly, the resultant materials were placed into a 6.0 M KOH solution and left for 12 h.

Material Characterizations. The crystalline structure of the materials was determined by X-ray powder diffraction (XRD, Ultima IV) at 45 kV with $\text{Cu K}\alpha$ radiation ($\lambda = 1.541874 \text{ \AA}$) at a scan rate of 5° min^{-1} . The elemental composition and oxidation states were analyzed by X-ray photoelectron spectroscopy (XPS) using an ESCALAB 250Xi instrument (Thermo Fisher Scientific) equipped with $\text{Al K}\alpha$ X-rays (1486.6 eV). The surface morphology and elemental composition of the resultant materials were evaluated using field emission scanning electron microscopy (FESEM, Navo Nano SEM450). The nitrogen adsorption/desorption isotherms, pore size distribution, and volume were obtained by using an ASAP 2460 instrument from Micromeritics at 77 K. The mechanical properties of the gel PVA membranes were tested on a material testing machine (Instron 5969). Water contact angles were measured on a Dataphysics OCA20 to assess wettability.

Electrochemical Measurements. The electrochemical performance was assessed using a CHI 760E electrochemical workstation with a standard two-electrode system in 6.0 M KOH. The alkaline electrolyzer with a $1 \times 1 \text{ cm}^2$ reaction area was custom-built for this

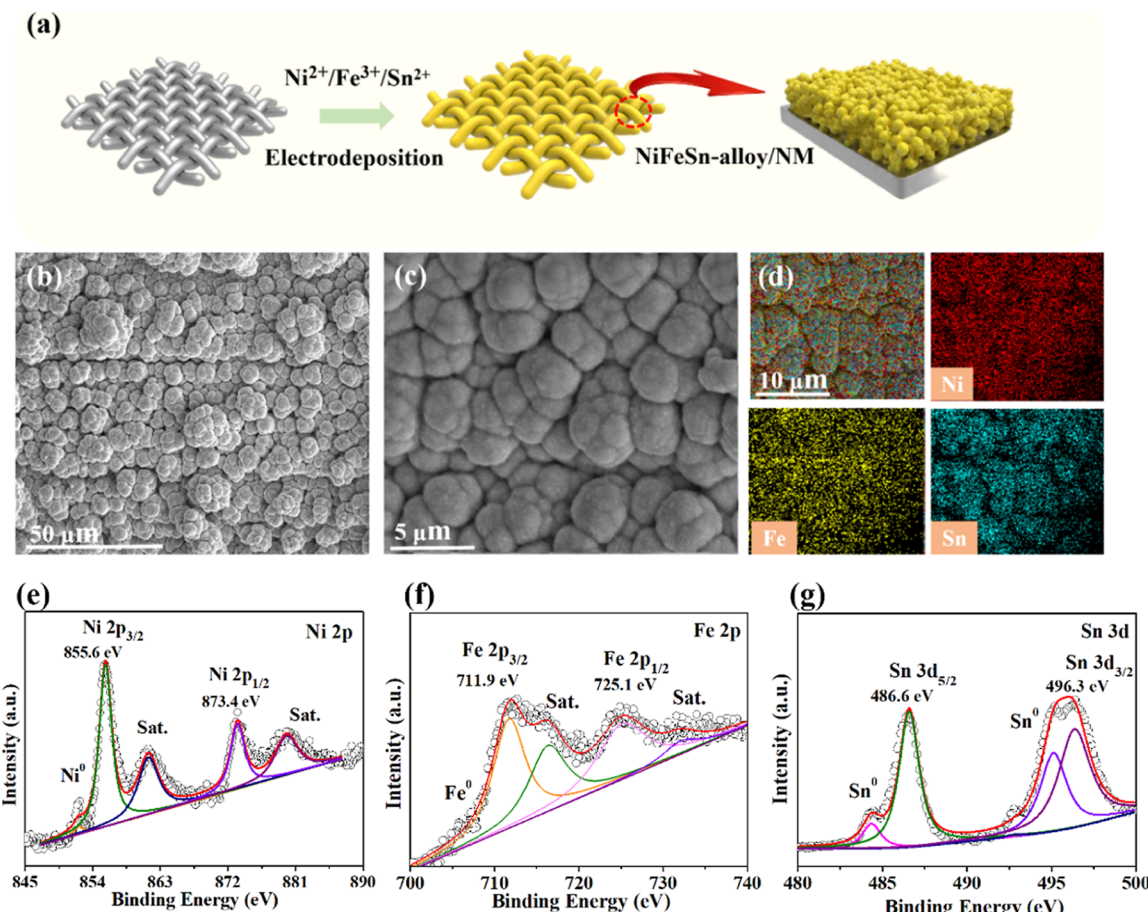


Figure 1. (a) Schematic illustration for the preparation of NiFeSn-alloy/NM via electrodeposition; (b,c) SEM images and corresponding (d) elemental mapping; and XPS spectrum of (e) Ni 2p, (f) Fe 2p, and (g) Sn 3d for NiFeSn-alloy/NM.

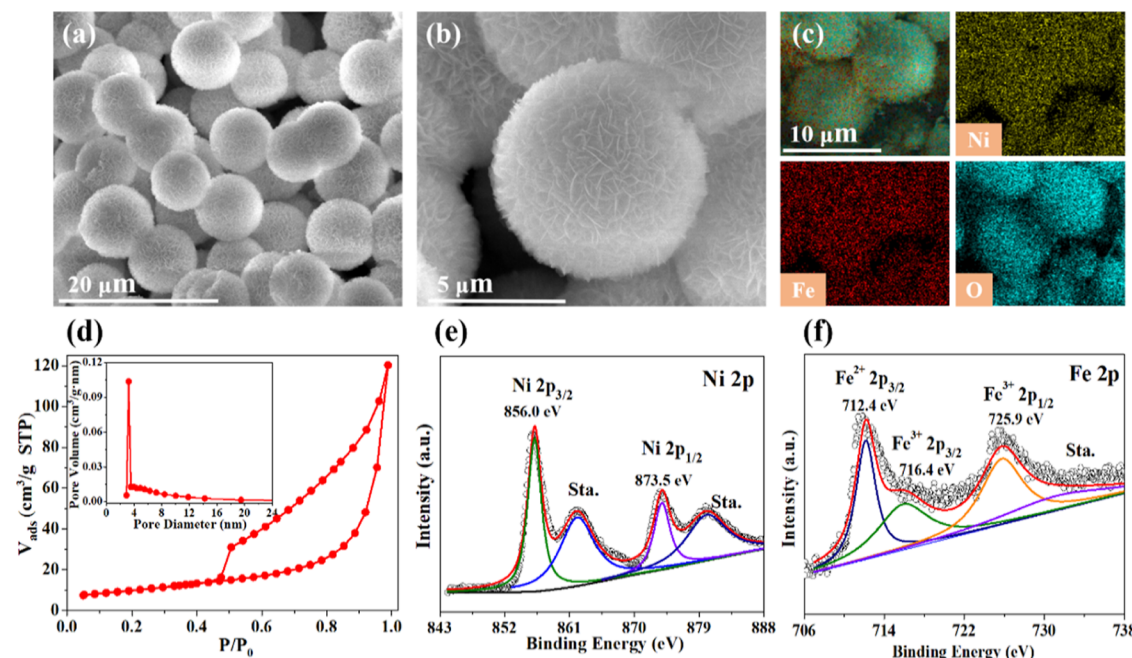


Figure 2. (a,b) SEM images of NiFe-LDH at different magnifications and corresponding (c) elemental mapping; (d) N₂ adsorption/desorption isotherm and pore size distribution curve; and XPS spectrum of (e) Ni 2p and (f) Fe 2p for NiFe-LDH sample.

experiment. The water-splitting device was assembled with NiFeSn-alloy/NM and NiFe-LDH/CC serving as the cathode and anode,

respectively, while a piece of the gel PVA membrane was utilized as the separator. An approximate amount of catalyst loadings for the

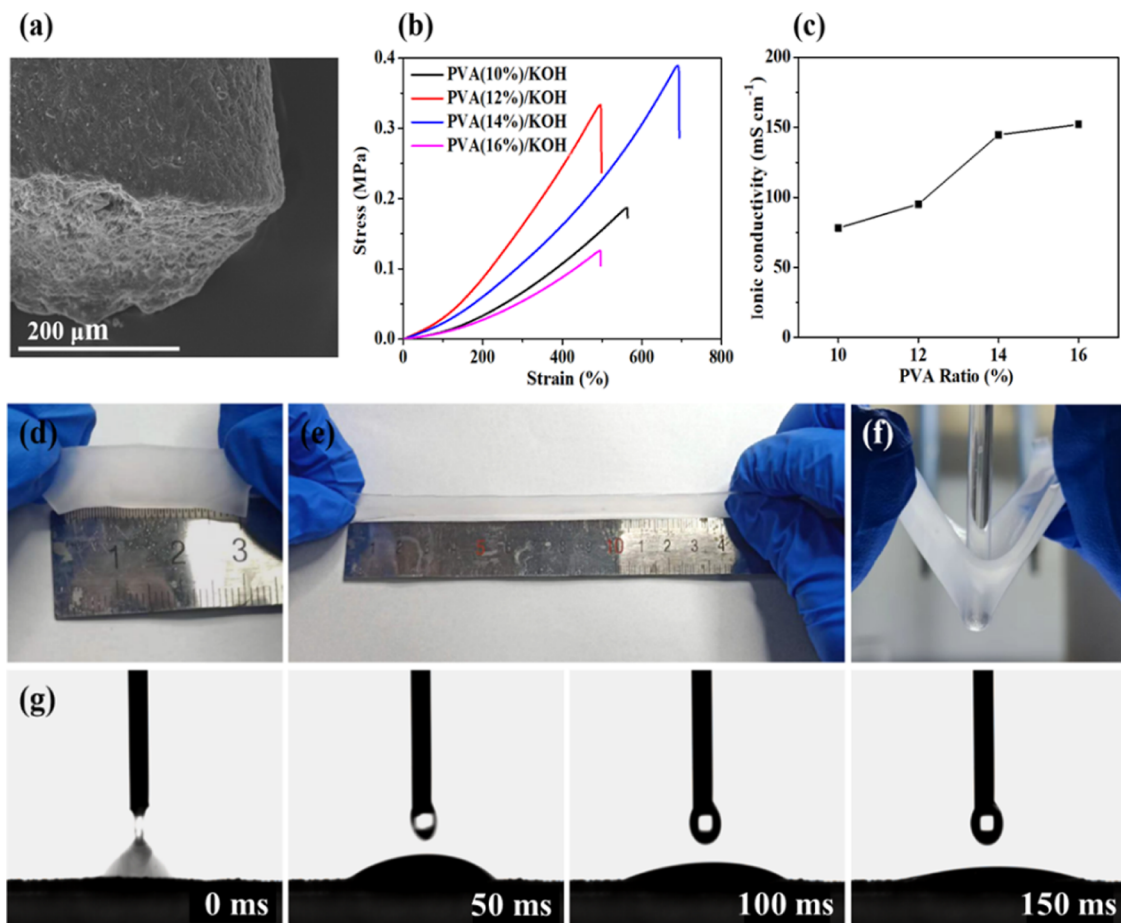


Figure 3. (a) SEM image of pure PVA gel membrane; (b) typical tensile stress–strain curves and the corresponding (c) ionic conductivity; (d,e) photos of the PVA gel membrane, stretching to 200%; (f) poking test; and (g) time-dependent contact angle measurements.

NiFeSn-alloy/NM and NiFe-LDH/CC were provided through the three groups' measurement datum and got a group result. As shown in Table S1, the average loadings of NiFeSn-alloy/NM and NiFe-LDH/CC were 4.12 and 0.59 mg cm⁻², respectively. The overall water splitting performance was tested by linear sweep voltammetry (LSV) and chronopotentiometry measurements.

RESULTS AND DISCUSSION

Figure 1a represents a schematic illustration of the synthesis process of the cathode. Briefly, the NiFeSn-alloy nanoparticles were electrodeposited on a NM surface in the presence of a solution containing metallic ions (Ni^{2+} , Fe^{3+} , and Sn^{2+}). As shown in Figure 1b,c, the resultant NiFeSn-alloy/NM electrode's surface consists of a multitude of nanoparticles, each with an approximate diameter of 5 μm . We observed an abundance of pore structures within these microspheres, which promote the exposure of catalytic active sites and expedite the diffusion of reaction-generated bubbles. Figure 1d displays the element distribution map of the NiFeSn-alloy/NM surface, indicating a uniform dispersion of Ni, Fe, and Sn within the particles. As shown in Figure S1, the XRD results reveal the prominent diffraction peaks of the NiFeSn-alloy, and the dominant diffraction peaks observed at 44.2, 51.5, and 75.5° correspond to the (111), (200), and (220) crystal faces of Ni (PDF # 04-0850), respectively. The XPS survey spectrum (Figure S2) for NiFeSn-alloy/NM provides further evidence of the presence of Ni, Fe, and Sn elements. Distinctly, the Ni 2p XPS spectrum can be deconvolved into four separate peaks

(Figure 1e). The two peaks at binding energies of 855.6 and 873.4 eV can be associated with Ni^{2+} , further accompanied by two satellite peaks oscillating at 861.9 and 879.8 eV. A characteristic signature of metallic Ni^0 can be observed at energy of 852.3 eV.^{52–54} This information demonstrates the coexistence of Ni^{2+} and Ni^0 on the NiFeSn-alloy/NM electrode surface. The Fe 2p spectrum (Figure 1f) presents two broad peaks at 711.9 and 725.1 eV, associated with Fe 2p_{3/2} and Fe 2p_{1/2}, respectively. The presence of a satellite peak can be assigned to the Fe^{2+} oxidation state, thereby indicating that Fe exists in the forms of the Fe^{2+} and Fe^{3+} oxidation state.^{55,56} Further scrutiny of the Sn 3d binding energy (Figure 1g) leads to deconvolution into peaks at 486.6 eV ($\text{Sn } 3\text{d}_{5/2}$) and 496.3 eV ($\text{Sn } 3\text{d}_{3/2}$). Peaks at the binding energies of 884.3 eV and 495.1 are attributed to metallic Sn^0 .⁵⁷ The XPS results together suggest that the NiFeSn-alloy/NM electrode surface is a composition of both metal alloy and metal oxide states, with the latter likely due to air exposure.

For the anode materials, the self-supported NiFe-LDH nanoparticles were synthesized by a facile hydrothermal treatment. As shown in Figure 2a,b, the SEM images of NiFe-LDH reveal the presence of numerous nanosheets arranged in a regular spherical structure with an average diameter of approximately 10 μm . This structure, with a large specific surface area and pore size, is relatively convenient for offering active sites during the electrolysis of water. Figure 2c displays the elemental mapping of NiFe-LDH, illustrating the uniform distribution of Ni, Fe, and O on the surface, and the

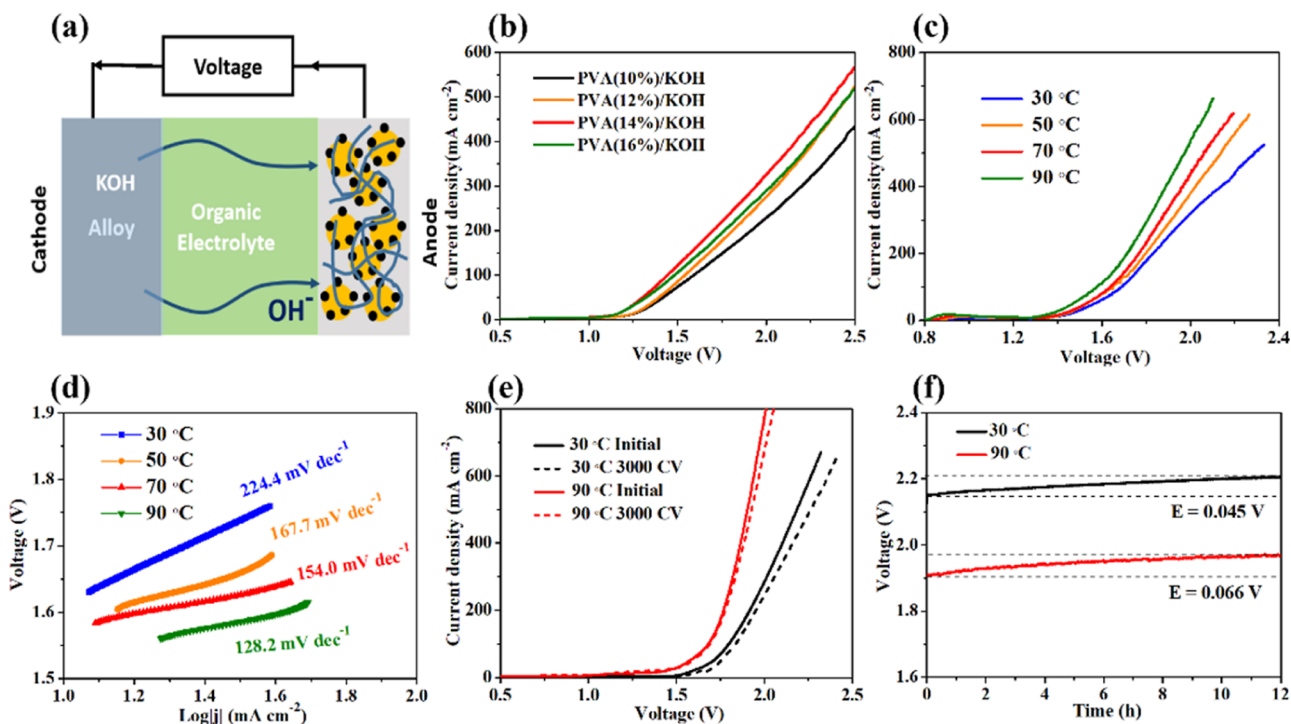


Figure 4. (a) Schematic representation of the overall water-splitting process shows the rational electrolyte structure including NiFeSn-alloy/NM, PVA gel membrane, and NiFe-LDH catalyst; (b) electrocatalytic activities with a series of PVA gel membrane; (c) LSV curves using PVA (14%)/KOH at various temperatures and (d) corresponding Tafel plots; and (e) LSV curves recorded before and after 3000 cycles at 30 and 90 °C, respectively, and (f) corresponding chronopotentiometry curves.

contents are 21.4, 7.2, and 71.4%, respectively. The XRD pattern in Figure S3 confirms the successful hydrothermal preparation of NiFe-LDH, as evidenced by the observed diffraction peaks of NiFe-LD at 11.89, 23.68, 34.66, 39.34, and 46.92°, corresponding to the (003), (006), (012), (015), and (018) crystal planes of NiFe-LDH (PDF # 51-0463),⁵⁸ respectively. As shown in Figure 2d, the pore structure information on the NiFe-LDH nanospheres was characterized by N₂ adsorption/desorption. The typical type IV isotherm with a distinct hysteresis loop was observed, indicating an abundant mesoporous structure with a high specific surface area of 86.3 m² g⁻¹ and a pore volume of 0.36 cm³ g⁻¹. Besides, the pore size (inset of Figure 2d) shows that the sizes of the micropores are mainly concentrated at 3.65 nm. The porosity of the NiFe-LDH catalyst is beneficial for electrolyte, charge, and mass transport for electrocatalysis. The survey XPS image of the NiFe-LDH catalyst is shown in Figure S4. As shown in Figure 2e, the peaks of Ni 2p at the binding energies of 856.0 and 873.5 eV belong to Ni²⁺, while the other two satellite peaks at 861.4 and 880.4 eV are also present.⁵⁹ In the spectrum of Fe 2p (Figure 2f), the characteristic peak at a binding energy of 712.4 eV can be attributed to Fe²⁺, whereas the peaks at binding energies of 716.4 and 725.9 eV are assigned to Fe³⁺.⁶⁰ In the high-resolution O 1s spectrum (Figure S5), four signals are observed at 530.4, 531.3, 531.6, and 532.4 eV, representing oxygen atoms bound to metals, oxygen in the H—O bond, surface-adsorbed oxygen, and adsorbed molecular water, respectively.⁶¹

The gel PVA membrane was obtained by the freezing cross-linking method. As shown in Figure 3a, the SEM image of pure PVA membrane from the cross-section exhibits significant compactness without any defect. As shown in Figure 3b, the gel PVA (14%)/KOH membrane possesses a relatively low

elastic modulus of 390 kPa with a large fracture strain of 700% by tensile stress-strain tests. As shown in Figure 3c, the resistance of PVA gels with different contents is obtained by the EIS test at a relative open-circuit potential of 0 V, and then the conductivity is calculated. The conductivity of the PVA gels increases with the increase of PVA content; when the PVA contents were 10, 12, 14, and 16 wt %, the conductivity was 78, 95, 144, and 152 mS cm⁻¹, respectively. Among the electrolyzers employing PVA gel membranes, the gel PVA (14%)/KOH membrane exhibited the lowest charge transfer resistance. This characteristic can potentially contribute to the enhancement of electrolyzed water performance, thereby highlighting one of its advantages. To verify stretchability, as shown in Figure 3d,e, the gel PVA (14%)/KOH membrane with a size of 2 × 3 cm² (thickness of 1.0 mm) was stretched (200%), and without any visible breakage. Moreover, this material passed the puncture test in Figure 3f to destruct vertical stretching without any visible cracks or breakage. The surface wettability was investigated by contact angle tests (Figure 3g), showing that the water droplet rapidly spread across the surface in only 150 ms. These results demonstrate the super hydrophilic nature of the gel PVA (14%)/KOH membrane, which facilitates swift diffusion and mass transfer of the electrolyte.

The electrolyzed water performance of the gel PVA membrane was evaluated using a custom-made electrolytic cell, as depicted in Figure 4a. The cell configuration incorporated NiFeSn-alloy/NM and NiFe-LDH/CC as the cathode and anode, respectively. Throughout the water electrolysis process, a 6.0 M KOH solution was introduced on the cathode side. The anodic reaction exclusively utilized OH⁻ ions transmitted from the cathode. Moreover, the anode was exposed to air to facilitate the release of the bubbles during

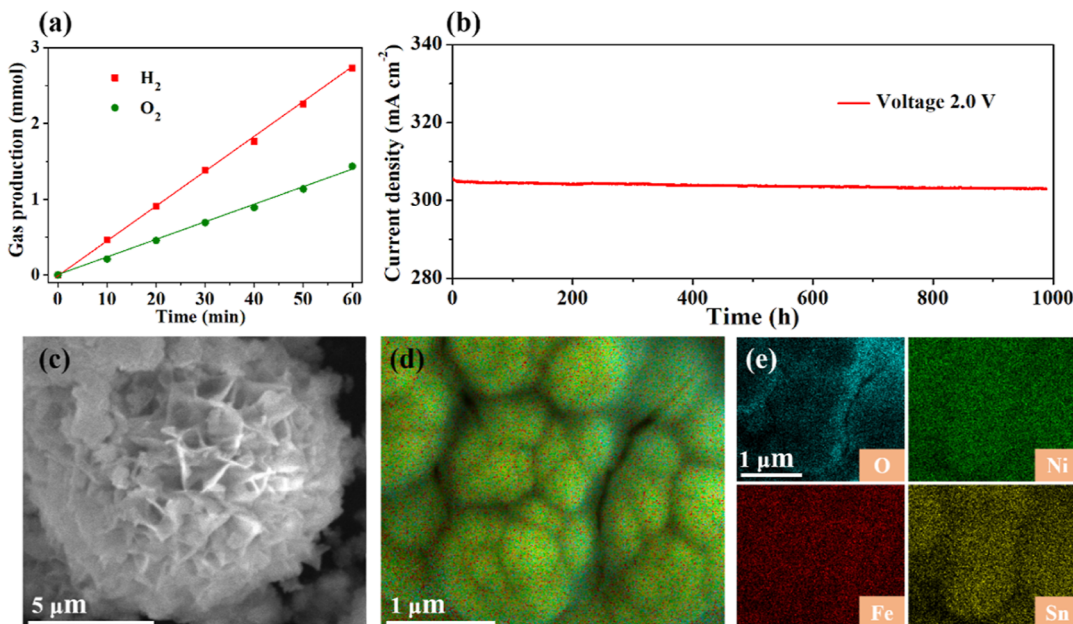


Figure 5. (a) Drainage method recorded the amount of H₂ and O₂ and the water-splitting device driven by a constant voltage at 2.0 V; (b) long-term stability with a constant potential of 2.0 V; (c) SEM image of NiFe-LDH after 1000 h; and (d,e) SEM image and elemental mapping of NiFeSn-alloy/NM after 1000 h.

electrolysis. This electrolyzer's unique structure, displayed in Figure 4b, demonstrates that an increase in PVA mass results in enhanced catalytic performance. The gel PVA (14%)/KOH membrane achieved a current density of 360 mA cm⁻² at a working voltage of 2.0 V. As shown in Figure S6 and Table S2, the results were also compared with those of similar materials and proved to be better. However, increasing the PVA concentration to 16% resulted in a slightly lower current density of 320 mA cm⁻². Further investigation is needed into the influence of reaction temperature on electrocatalytic activity offered insights into the water electrolysis reaction mechanism. As depicted in Figure 4c, the electrocatalytic performance of the system employing gel PVA (14%)/KOH membrane as the separator improved consistently with the temperature rise. Current densities ranged from 338 mA cm⁻² (30 °C) to 384 mA cm⁻² (50 °C), 448 mA cm⁻² (70 °C), and 552 mA cm⁻² (90 °C), indicating the pivotal role of the reaction temperature in the electrocatalytic process of water electrolysis. The corresponding Tafel slope, as shown in Figure 4d, decreased from 224.4 mV dec⁻¹ at 30 °C to 128.2 mV dec⁻¹ at 90 °C, suggesting a shift toward more favorable reaction kinetics in the Volmer step of H₂O and desorption step of O₂. Further stability testing was conducted at 30 and 90 °C (Figure 4e) involved CV sweeps within a potential region from 1.5 to 1.8 V. The system showed negligible decay even after 3000 continuous CV cycles. Chronopotentiometry curves, recorded at a current density of 400 mA cm⁻² and presented in Figure 4f, maintained a stable state for 12 h, experiencing only a slight voltage rise. This innovative electrolyzer structure affords obvious stability advantages owing to highly active catalytic electrodes and gas diffusion design on the anodic side. Moreover, this stability is further enhanced by the gel PVA membrane, which provides effective anion and mass transport channels.

The Faraday efficiency, another key performance indicator, was thoroughly evaluated at a constant voltage of 2.0 V by measuring H₂ and O₂ production at room temperature. As

shown in Figure 5a, nearly 100% Faraday efficiency was verified based on the gas content of H₂ and O₂ volume, underlining the high utilization of electrochemical charge during overall water splitting. Electrochemical stability is another important benchmark in evaluating the effectiveness of electrolyzed water. As shown in Figure 5b, no significant performance degradation was observed at the set voltage of 2.0 V, even after 1000 h of operation. This longevity underscores the durability of the NiFeSn-alloy/NM, NiFe-LDH/CC, and gel PVA membranes within the comprehensive water-splitting apparatus. Furthermore, Figure 5c presents the SEM image of NiFe-LD, which shows negligible changes even after extended testing over 1000 h, maintaining its initial nanosheet structure. For the cathode material, NiFeSn-alloy/NM, the electrode composite also maintained a complete morphology and structure, as shown in Figure 5d. The corresponding element mappings (Figure 5e) demonstrate that Ni, Fe, and Sn are uniformly distributed and preserved. These findings suggest that this innovative electrolyzer possesses promising potential for use in alkaline electrolyzed water applications.

CONCLUSIONS

In summary, we have designed a novel electrolyzer structure based on highly active and stable HER/OER electrodes of NiFeSn-alloy/NM and NiFe-LDH/CC. These optimum catalysts exhibit superior activity, contributing to their unique morphology and electronic structure, which enable rapid charge transport, increased access to active sites for electrolytes, and synergistic effects of composition. Besides, we adopted a gel PVA membrane, notable for its stretchability, adhesion, self-healing properties, and high conductivity. The membrane exhibited outstanding performance retention, withstanding strains of up to 650%, further facilitating the development of our integrated device. When employing NiFeSn-alloy/NM and NiFe-LDH/CC as anode and cathode for overall water splitting, we achieved a current density of 308 mA cm⁻² at 2.0 V, as well as superior stability for 1000 h.

These achievements not only prove the capacity for an ultralow cell voltage at 90 °C but also attest to an almost 100% Faradaic yield, suggesting great potential for this novel electrolyzer in sustainable energy applications.

■ ASSOCIATED CONTENT

Supporting Information

The Supporting Information is available free of charge at <https://pubs.acs.org/doi/10.1021/acs.langmuir.4c02126>.

Average loadings of NiFeSn-alloy/NM and NiFe-LDH/CC; XRD pattern of NiFeSn-alloy/NM electrode; XPS survey spectrum of NiFeSn-alloy/NM; XRD pattern of NiFe-LDH catalyst; XPS survey spectrum of NiFe-LDH catalyst; high-resolution O 1s spectra of NiFe-LDH catalyst; comparison of the alkaline water-splitting performance of NiFeSn-alloy/NM||NiFe-LDH/CC with other reported materials; and comparison of the alkaline water-splitting performance of NiFeSn-alloy/NM||NiFe-LDH/CC with other reported materials ([PDF](#))

■ AUTHOR INFORMATION

Corresponding Authors

Fajun Li – MOE Key Laboratory of Mesoscopic Chemistry, MOE Key Laboratory of High Performance Polymer Materials and Technology, Jiangsu Key Laboratory of Advanced Organic Materials, School of Chemistry and Chemical Engineering, Nanjing University, Nanjing 210023, China; Anhui Key Laboratory of Spin Electron and Nanomaterials, School of Chemistry and Chemical Engineering, Suzhou University, Suzhou 234000, PR China;  orcid.org/0000-0001-9942-3844; Email: lifajuncl2012@163.com

Haifeng Xu – Anhui Key Laboratory of Spin Electron and Nanomaterials, School of Chemistry and Chemical Engineering, Suzhou University, Suzhou 234000, PR China; Email: xuhafeng@ahsuzu.edu.cn

Zhong Jin – MOE Key Laboratory of Mesoscopic Chemistry, MOE Key Laboratory of High Performance Polymer Materials and Technology, Jiangsu Key Laboratory of Advanced Organic Materials, School of Chemistry and Chemical Engineering, Nanjing University, Nanjing 210023, China;  orcid.org/0000-0001-8860-8579; Email: zhongjin@nju.edu.cn

Authors

Huaizhu Wang – MOE Key Laboratory of Mesoscopic Chemistry, MOE Key Laboratory of High Performance Polymer Materials and Technology, Jiangsu Key Laboratory of Advanced Organic Materials, School of Chemistry and Chemical Engineering, Nanjing University, Nanjing 210023, China

Guizhi Wang – Anhui Key Laboratory of Spin Electron and Nanomaterials, School of Chemistry and Chemical Engineering, Suzhou University, Suzhou 234000, PR China

Min Ding – Anhui Key Laboratory of Spin Electron and Nanomaterials, School of Chemistry and Chemical Engineering, Suzhou University, Suzhou 234000, PR China

Qihui Ma – Anhui Key Laboratory of Spin Electron and Nanomaterials, School of Chemistry and Chemical Engineering, Suzhou University, Suzhou 234000, PR China

Complete contact information is available at:

<https://pubs.acs.org/10.1021/acs.langmuir.4c02126>

Notes

The authors declare no competing financial interest.

■ ACKNOWLEDGMENTS

This work was supported by the National Key R&D Program of China (2017YFA0208200), the National Natural Science Foundation of China (22022505 and 21872069), the Fundamental Research Funds for the Central Universities of China (020514380266, 020514380272, and 020514380274), the Natural Science Research Project and Quality Engineering Projects of Anhui Provincial Education Department (2108085MB67, 2022AH040209, and 2022zybj094), the Scientific Research Platform of Suzhou University (2021XJPT07), and the Scientific and Technological Innovation Special Fund for Carbon Peak and Carbon Neutrality of Jiangsu Province (BK20220008). This work was also supported by Anhui Province Young Backbone Teachers' In-country Study Visit Programme (JNFX2023067).

■ REFERENCES

- (1) Zhao, X.; Tang, K.; Wang, X.; Qi, W.; Yu, H.; Du, C.-F.; Ye, Q. A self-supported bifunctional MoNi₄ framework with iron doping for ultra-efficient water splitting. *J. Mater. Chem. A* **2023**, *11*, 3408–3417.
- (2) Zhang, R.; Li, Y.; Zhou, X.; Yu, A.; Huang, Q.; Xu, T.; Zhu, L.; Peng, P.; Song, S.; Echegoyen, L.; Li, F. F. Single-atomic platinum on fullerene C₆₀ surfaces for accelerated alkaline hydrogen evolution. *Nat. Commun.* **2023**, *14* (1), 2460.
- (3) Wang, J.; Xu, F.; Jin, H.; Chen, Y.; Wang, Y. Non-Noble Metal-based Carbon Composites in Hydrogen Evolution Reaction: Fundamentals to Applications. *Adv. Mater.* **2017**, *29* (14), 1605838.
- (4) Suen, N.-T.; Hung, S.-F.; Quan, Q.; Zhang, N.; Xu, Y.-J.; Chen, H. M. Electrocatalysis for the oxygen evolution reaction: recent development and future perspectives. *Chem. Soc. Rev.* **2017**, *46* (2), 337–365.
- (5) Wang, Q.; O'Hare, D. Recent Advances in the Synthesis and Application of Layered Double Hydroxide (LDH) Nanosheets. *Chem. Rev.* **2012**, *112* (7), 4124–4155.
- (6) Zheng, Y.; Jiao, Y.; Vasileff, A.; Qiao, S.-Z. The Hydrogen Evolution Reaction in Alkaline Solution: From Theory, Single Crystal Models, to Practical Electrocatalysts. *Angew. Chem., Int. Ed.* **2018**, *57* (26), 7568–7579.
- (7) Kim, J. S.; Kim, B.; Kim, H.; Kang, K. Recent Progress on Multimetal Oxide Catalysts for the Oxygen Evolution Reaction. *Adv. Energy Mater.* **2018**, *8* (11), 1702774.
- (8) Wang, C.; Qi, L. Heterostructured Inter-Doped Ruthenium–Cobalt Oxide Hollow Nanosheet Arrays for Highly Efficient Overall Water Splitting. *Angew. Chem., Int. Ed.* **2020**, *59* (39), 17219–17224.
- (9) Li, Y.; Li, F.; Zhao, Y.; Li, S.-N.; Zeng, J.-H.; Yao, H.-C.; Chen, Y. Iron doped cobalt phosphide ultrathin nanosheets on nickel foam for overall water splitting. *J. Mater. Chem. A* **2019**, *7* (36), 20658–20666.
- (10) Vij, V.; Sultan, S.; Harzandi, A. M.; Meena, A.; Tiwari, J. N.; Lee, W.-G.; Yoon, T.; Kim, K. S. Nickel-Based Electrocatalysts for Energy-Related Applications: Oxygen Reduction, Oxygen Evolution, and Hydrogen Evolution Reactions. *ACS Catal.* **2017**, *7* (10), 7196–7225.
- (11) Suntivich, J.; May, K. J.; Gasteiger, H. A.; Goodenough, J. B.; Shao-Horn, Y. A Perovskite Oxide Optimized for Oxygen Evolution Catalysis from Molecular Orbital Principles. *Science* **2011**, *334* (6061), 1383–1385.
- (12) Wei, R.; Gu, Y.; Zou, L.; Xi, B.; Zhao, Y.; Ma, Y.; Qian, Y.; Xiong, S.; Xu, Q. Nanoribbon Superstructures of Graphene Nanocages for Efficient Electrocatalytic Hydrogen Evolution. *Nano Lett.* **2020**, *20* (10), 7342–7349.

- (13) Zhu, K.; Chen, J.; Wang, W.; Liao, J.; Dong, J.; Chee, M. O. L.; Wang, N.; Dong, P.; Ajayan, P. M.; Gao, S.; Shen, J.; Ye, M. Etching-Doping Sedimentation Equilibrium Strategy: Accelerating Kinetics on Hollow Rh-Doped CoFe-Layered Double Hydroxides for Water Splitting. *Adv. Funct. Mater.* **2020**, *30* (35), 2003556.
- (14) Zhang, Y.; Li, Z.; Hou, L.; Liu, X. Thermal Shrinkage Engineering Enables Electrocatalysts for Stable Hydrogen Evolution at 2000 mA cm⁻². *Adv. Funct. Mater.* **2023**, *33*, 2213976.
- (15) Zhang, C.; Xu, Z.; Han, N.; Tian, Y.; Kallio, T.; Yu, C.; Jiang, L. Superaerophilic/superaerophobic cooperative electrode for efficient hydrogen evolution reaction via enhanced mass transfer. *Sci. Adv.* **2023**, *9* (3), No. eadd6978.
- (16) Liu, H.; Yang, D.-H.; Wang, X.-Y.; Zhang, J.; Han, B.-H. N-doped graphitic carbon shell-encapsulated FeCo alloy derived from metal–polyphenol network and melamine sponge for oxygen reduction, oxygen evolution, and hydrogen evolution reactions in alkaline media. *J. Colloid Interface Sci.* **2021**, *581*, 362–373.
- (17) Merki, D.; Vrubel, H.; Rovelli, L.; Fierro, S.; Hu, X. Fe, Co, and Ni ions promote the catalytic activity of amorphous molybdenum sulfide films for hydrogen evolution. *Chem. Sci.* **2012**, *3* (8), 2515–2525.
- (18) Hong, S. H.; Ahn, S. H.; Choi, I.; Pyo, S. G.; Kim, H.-J.; Jang, J. H.; Kim, S.-K. Fabrication and evaluation of nickel cobalt alloy electrocatalysts for alkaline water splitting. *Appl. Surf. Sci.* **2014**, *307*, 146–152.
- (19) Hung, T.-F.; Yin, Z.-W.; Betzler, S. B.; Zheng, W.; Yang, J.; Zheng, H. Nickel sulfide nanostructures prepared by laser irradiation for efficient electrocatalytic hydrogen evolution reaction and supercapacitors. *Chem. Eng. J.* **2019**, *367*, 115–122.
- (20) Ji, X.; Lin, Y.; Zeng, J.; Ren, Z.; Lin, Z.; Mu, Y.; Qiu, Y.; Yu, J. Graphene/MoS₂/FeCoNi(OH)_x and Graphene/MoS₂/FeCoNiP_x multilayer-stacked vertical nanosheets on carbon fibers for highly efficient overall water splitting. *Nat. Commun.* **2021**, *12* (1), 1380.
- (21) Lin, Y.; Yu, M.; Fan, T. Insights into mechanisms of pranoprofen-induced apoptosis and necroptosis in human corneal stromal cells. *Toxicol. Lett.* **2020**, *320*, 9–18.
- (22) Cai, Z.; Zhou, D.; Wang, M.; Bak, S.-M.; Wu, Y.; Wu, Z.; Tian, Y.; Xiong, X.; Li, Y.; Liu, W.; Siahrostami, S.; Kuang, Y.; Yang, X.-Q.; Duan, H.; Feng, Z.; Wang, H.; Sun, X. Introducing Fe²⁺ into Nickel–Iron Layered Double Hydroxide: Local Structure Modulated Water Oxidation Activity. *Angew. Chem., Int. Ed.* **2018**, *57* (30), 9392–9396.
- (23) Guo, Z.; Ye, W.; Fang, X.; Wan, J.; Ye, Y.; Dong, Y.; Cao, D.; Yan, D. Amorphous cobalt–iron hydroxides as high-efficiency oxygen-evolution catalysts based on a facile electrospinning process. *Inorg. Chem. Front.* **2019**, *6* (3), 687–693.
- (24) Thangavel, P.; Kim, G.; Kim, K. S. Electrochemical integration of amorphous NiFe (oxy)hydroxides on surface-activated carbon fibers for high-efficiency oxygen evolution in alkaline anion exchange membrane water electrolysis. *J. Mater. Chem. A* **2021**, *9* (24), 14043–14051.
- (25) Song, F.; Hu, X. Exfoliation of layered double hydroxides for enhanced oxygen evolution catalysis. *Nat. Commun.* **2014**, *5* (1), 4477.
- (26) Ping, J.; Wang, Y.; Lu, Q.; Chen, B.; Chen, J.; Huang, Y.; Ma, Q.; Tan, C.; Yang, J.; Cao, X.; Wang, Z.; Wu, J.; Ying, Y.; Zhang, H. Self-Assembly of Single-Layer CoAl-Layered Double Hydroxide Nanosheets on 3D Graphene Network Used as Highly Efficient Electrocatalyst for Oxygen Evolution Reaction. *Adv. Mater.* **2016**, *28* (35), 7640–7645.
- (27) Burke, M. S.; Zou, S.; Enman, L. J.; Kellon, J. E.; Gabor, C. A.; Pledger, E.; Boettcher, S. W. Revised Oxygen Evolution Reaction Activity Trends for First-Row Transition-Metal (Oxy)hydroxides in Alkaline Media. *J. Phys. Chem. Lett.* **2015**, *6* (18), 3737–3742.
- (28) Wang, H.; Zhou, T.; Li, P.; Cao, Z.; Xi, W.; Zhao, Y.; Ding, Y. Self-Supported Hierarchical Nanostructured NiFe-LDH and Cu₃P Weaving Mesh Electrodes for Efficient Water Splitting. *ACS Sustainable Chem. Eng.* **2018**, *6* (1), 380–388.
- (29) Zhang, H.; Li, X.; Hänel, A.; Naumann, V.; Lin, C.; Azimi, S.; Schweizer, S. L.; Maijenburg, A. W.; Wehrspohn, R. B. Bifunctional Heterostructure Assembly of NiFe LDH Nanosheets on NiCoP Nanowires for Highly Efficient and Stable Overall Water Splitting. *Adv. Funct. Mater.* **2018**, *28* (14), 1706847.
- (30) Hu, L.; Zeng, X.; Wei, X.; Wang, H.; Wu, Y.; Gu, W.; Shi, L.; Zhu, C. Interface engineering for enhancing electrocatalytic oxygen evolution of NiFe LDH/NiTe heterostructures. *Appl. Catal., B* **2020**, *273*, 119014.
- (31) Zavala, L. A.; Kumar, K.; Martin, V.; Maillard, F.; Maugé, F.; Portier, X.; Oliviero, L.; Dubau, L. Direct Evidence of the Role of Co or Pt, Co Single-Atom Promoters on the Performance of MoS₂ Nanoclusters for the Hydrogen Evolution Reaction. *ACS Catal.* **2023**, *13* (2), 1221–1229.
- (32) Zhou, Q.; Li, T.-T.; Qian, J.; Xu, W.; Hu, Y.; Zheng, Y.-Q. CuO Nanorod Arrays Shelled with Amorphous NiFe Layered Double Hydroxide Film for Enhanced Electrocatalytic Water Oxidation Activity. *ACS Appl. Energy Mater.* **2018**, *1* (3), 1364–1373.
- (33) Li, Y.; Zhang, X.; Hu, A.; Li, M. Morphological variation of electrodeposited nanostructured Ni-Co alloy electrodes and their property for hydrogen evolution reaction. *Int. J. Hydrol. Energy* **2018**, *43* (49), 22012–22020.
- (34) Gao, D.; Guo, J.; He, H.; Xiao, P.; Zhang, Y. Geometric and electronic modulation of fcc NiCo alloy by Group-VI B metal doping to accelerate hydrogen evolution reaction in acidic and alkaline media. *Chem. Eng. J.* **2022**, *430*, 133110.
- (35) Narani, A.; Chowdari, R. K.; Cannilla, C.; Bonura, G.; Frusteri, F.; Heeres, H. J.; Barta, K. Efficient catalytic hydrotreatment of Kraft lignin to alkylphenolics using supported NiW and NiMo catalysts in supercritical methanol. *Green Chem.* **2015**, *17* (11), 5046–5057.
- (36) Fosdick, S. E.; Berglund, S. P.; Mullins, C. B.; Crooks, R. M. Evaluating Electrocatalysts for the Hydrogen Evolution Reaction Using Bipolar Electrode Arrays: Bi- and Trimetallic Combinations of Co, Fe, Ni, Mo, and W. *ACS Catal.* **2014**, *4* (5), 1332–1339.
- (37) Wang, J.; Xin, S.; Xiao, Y.; Zhang, Z.; Li, Z.; Zhang, W.; Li, C.; Bao, R.; Peng, J.; Yi, J.; Chou, S. Manipulating the Water Dissociation Electrocatalytic Sites of Bimetallic Nickel-Based Alloys for Highly Efficient Alkaline Hydrogen Evolution. *Angew. Chem., Int. Ed.* **2022**, *61* (30), No. e202202518.
- (38) Lai, C.; Zhou, H.; Ji, S.; Guo, Z.; Sun, J.; Wang, H.; Nie, L.; Zhang, D.; Li, F.; Lei, L. A hierarchical nickel–iron hydroxide nanosheet from the high voltage cathodic polarization for alkaline water splitting. *Int. J. Hydrol. Energy* **2022**, *47* (81), 34421–34429.
- (39) Li, F.; Jiang, M.; Lai, C.; Xu, H.; Zhang, K.; Jin, Z. Yttrium- and Cerium-Codoped Ultrathin Metal-Organic Framework Nanosheet Arrays for High-Efficiency Electrocatalytic Overall Water Splitting. *Nano Lett.* **2022**, *22* (17), 7238–7245.
- (40) Zheng, X.; Han, X.; Cao, Y.; Zhang, Y.; Nordlund, D.; Wang, J.; Chou, S.; Liu, H.; Li, L.; Zhong, C.; Deng, Y.; Hu, W. Identifying Dense NiSe₂/CoSe₂ Heterointerfaces Coupled with Surface High-Valence Bimetallic Sites for Synergistically Enhanced Oxygen Electrocatalysis. *Adv. Mater.* **2020**, *32* (26), 2000607.
- (41) Zhang, G.; Feng, Y.-S.; Lu, W.-T.; He, D.; Wang, C.-Y.; Li, Y.-K.; Wang, X.-Y.; Cao, F.-F. Enhanced Catalysis of Electrochemical Overall Water Splitting in Alkaline Media by Fe Doping in Ni₃S₂ Nanosheet Arrays. *ACS Catal.* **2018**, *8* (6), 5431–5441.
- (42) Sun, T.; Cao, J.; Dong, J.; Du, H.; Zhang, H.; Chen, J.; Xu, L. Ordered mesoporous NiCo alloys for highly efficient electrocatalytic hydrogen evolution reaction. *Int. J. Hydrol. Energy* **2017**, *42* (10), 6637–6645.
- (43) Song, J.; Jin, Y. Q.; Zhang, L.; Dong, P.; Li, J.; Xie, F.; Zhang, H.; Chen, J.; Jin, Y.; Meng, H.; Sun, X. Phase-Separated Mo–Ni Alloy for Hydrogen Oxidation and Evolution Reactions with High Activity and Enhanced Stability. *Adv. Energy Mater.* **2021**, *11* (16), 2003511.
- (44) Zhou, J.; Yu, L.; Zhou, Q.; Huang, C.; Zhang, Y.; Yu, B.; Yu, Y. Ultrafast fabrication of porous transition metal foams for efficient electrocatalytic water splitting. *Appl. Catal., B* **2021**, *288*, 120002.
- (45) Teng, X.; Wang, J.; Ji, L.; Liu, Y.; Zhang, C.; Chen, Z. Fabrication of Three-Dimensional Multiscale Porous Alloy Foams at a Planar Substrate for Efficient Water Splitting. *ACS Sustainable Chem. Eng.* **2019**, *7* (5), 5412–5419.

- (46) Thangavel, P.; Ha, M.; Kumaraguru, S.; Meena, A.; Singh, A. N.; Harzandi, A. M.; Kim, K. S. Graphene-nanoplatelets-supported NiFe-MOF: high-efficiency and ultra-stable oxygen electrodes for sustained alkaline anion exchange membrane water electrolysis. *Energy Environ. Sci.* **2020**, *13* (10), 3447–3458.
- (47) Lai, C.; Ji, S.; Zhou, H.; Guo, Z.; Wang, H.; Sun, J.; Nie, L.; Zhang, D.; Li, F.; Lei, L. Multi-configuration structure based on catalysis electrodes and composite membrane for efficient alkaline water splitting. *Chem. Eng. J.* **2023**, *454*, 140373.
- (48) Zeng, K.; Zhang, D. Recent progress in alkaline water electrolysis for hydrogen production and applications. *Prog. Energy Combust. Sci.* **2010**, *36* (3), 307–326.
- (49) Stojić, D. L.; Marčeta, M. P.; Sovilj, S. P.; Miljanić, Š. S. Hydrogen generation from water electrolysis—possibilities of energy saving. *J. Power Sources* **2003**, *118* (1–2), 315–319.
- (50) Meena, A.; Thangavel, P.; Jeong, D. S.; Singh, A. N.; Jana, A.; Im, H.; Nguyen, D. A.; Kim, K. S. Crystalline-amorphous interface of mesoporous $\text{Ni}_2\text{P}@\text{FePO}_x\text{H}_y$ for oxygen evolution at high current density in alkaline-anion-exchange-membrane water-electrolyzer. *Appl. Catal., B* **2022**, *306*, 121127.
- (51) Chen, L.; Xu, Q.; Oener, S. Z.; Fabrizio, K.; Boettcher, S. W. Design principles for water dissociation catalysts in high-performance bipolar membranes. *Nat. Commun.* **2022**, *13* (1), 3846.
- (52) Yan, H.; Xie, Y.; Wu, A.; Cai, Z.; Wang, L.; Tian, C.; Zhang, X.; Fu, H. Anion-Modulated HER and OER Activities of 3D Ni–V-Based Interstitial Compound Heterojunctions for High-Efficiency and Stable Overall Water Splitting. *Adv. Mater.* **2019**, *31* (23), 1901174.
- (53) El Gabaly, F.; McCarty, K. F.; Bluhm, H.; McDaniel, A. H. Oxidation stages of Ni electrodes in solid oxide fuel cell environments. *Phys. Chem. Chem. Phys.* **2013**, *15* (21), 8334–8341.
- (54) Zhang, H.; Li, F.; Ji, S.; Yang, J.; Zhang, C.; Yang, F.; Lei, L. One-step electrodeposition of cauliflower-like Ni–Fe–Sn particles as a highly-efficient electrocatalyst for the hydrogen evolution reaction. *Int. J. Hydron. Energy* **2020**, *45* (46), 24615–24625.
- (55) Biesinger, M. C.; Payne, B. P.; Grosvenor, A. P.; Lau, L. W. M.; Gerson, A. R.; Smart, R. S. C. Resolving surface chemical states in XPS analysis of first row transition metals, oxides and hydroxides: Cr, Mn, Fe, Co and Ni. *Appl. Surf. Sci.* **2011**, *257* (7), 2717–2730.
- (56) Wang, Y.; Xie, C.; Zhang, Z.; Liu, D.; Chen, R.; Wang, S. In Situ Exfoliated, N-Doped, and Edge-Rich Ultrathin Layered Double Hydroxides Nanosheets for Oxygen Evolution Reaction. *Adv. Funct. Mater.* **2018**, *28* (4), 1703363.
- (57) Jaffery, H. A.; Mohd Sabri, M. F.; Rozali, S.; Mahdavifard, M. H.; Shnawah, D. A. Effect of temperature and alloying elements (Fe and Bi) on the electrical resistivity of Sn–0.7Cu solder alloy. *RSC Adv.* **2016**, *6* (63), 58010–58019.
- (58) Hui, L.; Xue, Y.; Huang, B.; Yu, H.; Zhang, C.; Zhang, D.; Jia, D.; Zhao, Y.; Li, Y.; Liu, H.; Li, Y. Overall water splitting by graphdiyne-exfoliated and -sandwiched layered double-hydroxide nanosheet arrays. *Nat. Commun.* **2018**, *9* (1), 5309.
- (59) Li, P.; Xu, T.; Ding, P.; Deng, J.; Zha, C.; Wu, Y.; Wang, Y.; Li, Y. Highly reversible Na and K metal anodes enabled by carbon paper protection. *Energy Storage Materials* **2018**, *15*, 8–13.
- (60) Long, X.; Li, J.; Xiao, S.; Yan, K.; Wang, Z.; Chen, H.; Yang, S. A Strongly Coupled Graphene and FeNi Double Hydroxide Hybrid as an Excellent Electrocatalyst for the Oxygen Evolution Reaction. *Angew. Chem., Int. Ed.* **2014**, *53* (29), 7584–7588.
- (61) Zhang, Q.; Bedford, N. M.; Pan, J.; Lu, X.; Amal, R. A Fully Reversible Water Electrolyzer Cell Made Up from FeCoNi (Oxy)-hydroxide Atomic Layers. *Adv. Energy Mater.* **2019**, *9* (29), 1901312.



CAS BIOFINDER DISCOVERY PLATFORM™

STOP DIGGING THROUGH DATA — START MAKING DISCOVERIES

CAS BioFinder helps you find the right biological insights in seconds

Start your search

